



Cite this: DOI: 10.1039/d5sc08787b

All publication charges for this article have been paid for by the Royal Society of Chemistry

## Controlled high-yield assembly of gold nanoparticles *via* amide bond formation

Seoyoung Hwang, Yeonsoo Lim, Sunbum Kwon \* and Sangwoon Yoon \*

Assembly of gold nanoparticles (AuNPs) enhances their plasmonic properties, including visible coloration, local electric field generation, hot-carrier production, and photothermal heating. While assembling AuNPs through chemical reactions that create solid, well-defined covalent linkages is highly desirable, achieving such assemblies with high efficiency remains challenging. During surface functionalisation and interparticle reactions, AuNPs are prone to aggregation, which compromises colloidal stability and yield. Such uncontrolled agglomeration can easily be mistaken for successful covalent assembly, because instability-driven clustering—and even nonspecific electrostatic association between oppositely charged particles—can produce structures that resemble the intended covalently bonded nanoassemblies. Here, we present a general strategy for assembling AuNPs through covalent amide linkages, providing detailed experimental guidelines and critical precautions to avoid these pitfalls and to achieve reproducible, high-yield assembly. To prevent aggregation during ligand exchange, AuNPs are immobilised on glass substrates and functionalised with amine groups (NH<sub>2</sub>-AuNPs). Alkylamines such as 6-amino-1-hexanethiol outperform arylamines because of their higher nucleophilicity towards activated carboxyl groups. We prepare carboxyl-functionalised AuNPs (COOH-AuNPs) by ligand exchange with mercaptoalkanoic acids and find that removing unbound ligands is essential for high-yield assembly. Hydrophilic discrete PEG spacers stabilise COOH-AuNPs during repeated centrifugation for purification. In the presence of EDC, NH<sub>2</sub>-AuNPs and COOH-AuNPs form covalently linked assemblies with yields of 95 ± 5%. The resulting nanoassemblies exhibit well-defined 1:1 or 1:2 core–satellite stoichiometries, reflecting the limited availability of activated carboxyl groups. Raman spectroscopy confirms the formation of interparticle amide bonds. Finally, we demonstrate that this method is broadly applicable to the high-yield assembly of AuNPs across diverse shapes (nanospheres, nanocubes, nanorods) and sizes (14–101 nm). This strategy provides a versatile platform for constructing plasmonic nanoassemblies with chemical reactions.

Received 11th November 2025  
Accepted 8th January 2026

DOI: 10.1039/d5sc08787b  
[rsc.li/chemical-science](http://rsc.li/chemical-science)

## Introduction

Gold nanoparticles (AuNPs) exhibit remarkable plasmonic properties.<sup>1</sup> A plasmon—a quasiparticle representing the collective oscillation of conduction electrons—gives rise to the bright visible coloration of AuNPs, strong local electric fields, hot-carrier generation, and photothermal heating.<sup>2–5</sup> These properties underpin a wide range of applications, including colorimetric sensing, surface-enhanced spectroscopy, photocatalysis, photovoltaics, and photothermal therapy.<sup>6–11</sup>

These effects are dramatically enhanced when AuNPs are assembled to form nanogaps.<sup>12</sup> Plasmon coupling between closely spaced nanoparticles broadens the accessible spectral range; nanogaps intensify local fields and promote hot-carrier generation.<sup>13–15</sup> Controlled assembly of AuNPs is therefore a key step toward advancing plasmonic applications.

The most straightforward approach to assemble nanoparticles is to introduce complementary functional groups that engage in specific molecular interactions (Fig. 1). Such interactions include electrostatic attraction between oppositely charged groups, hydrogen bonding (e.g., between DNA bases), and covalent bond formation *via* chemical reactions. Among these, covalent bonding is most desirable, as it provides strong and durable linkages, defines nanogap distances through fixed bond lengths, and allows reversible disassembly through selective bond cleavage.<sup>16</sup>

Despite these advantages, only a few chemical reactions have been exploited for nanoparticle assembly. Amide bond formation between amines and carboxyl groups is one of the most common strategies for conjugating antibodies and proteins to AuNP surfaces,<sup>17–19</sup> yet its use for forming interparticle linkages remains rare. Other high-yield organic reactions—such as Suzuki–Miyaura coupling and click chemistry—are also conceivable, but have been applied to nanoparticle assembly only sparingly.<sup>20–26</sup>

Department of Chemistry, Chung-Ang University, 84 Heukseok-ro, Dongjak-gu, Seoul 06974, South Korea. E-mail: [sangwoon@cau.ac.kr](mailto:sangwoon@cau.ac.kr); [skwon@cau.ac.kr](mailto:skwon@cau.ac.kr)



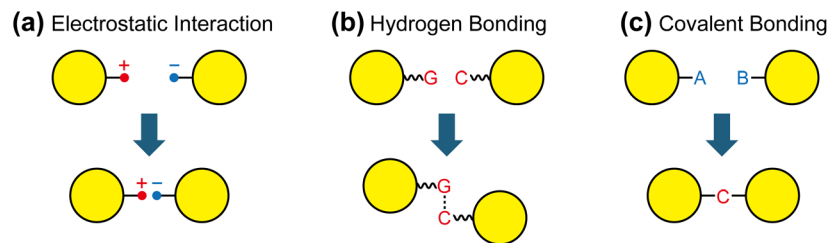
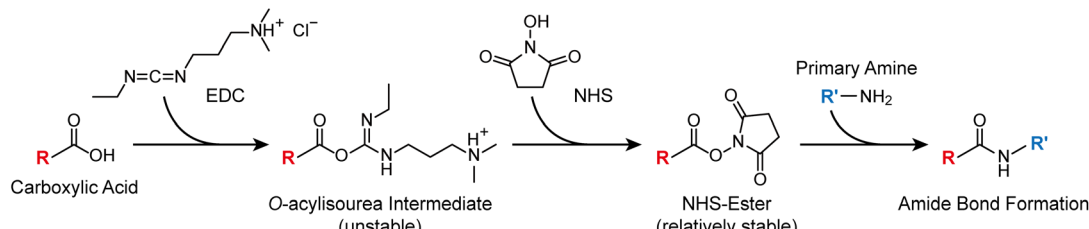


Fig. 1 Assembly of AuNPs through molecular interactions: (a) electrostatic attraction between oppositely charged surface groups (e.g.,  $-\text{NH}_3^+$ / $-\text{COO}^-$ ), (b) hydrogen bonding between complementary functional groups (e.g., DNA bases), and (c) covalent bond formation through chemical reactions between surface ligands.



Scheme 1 Amide bond formation between carboxyl and amine groups. The carboxyl group is first activated by EDC to form an unstable *O*-acylisourea intermediate, which reacts with NHS to generate a more stable NHS ester. This ester subsequently couples with a primary amine to yield the final amide bond.

The primary challenge in translating well-established organic reactions to nanoparticle assembly is maintaining colloidal stability. Nanoparticle surfaces are typically capped with ligands bearing charged groups (e.g.,  $-\text{NH}_3^+$ ,  $-\text{COO}^-$ ,  $-\text{SO}_3^-$ ), and the resulting electrostatic repulsion counteracts van der Waals attraction, stabilising the colloid in solution according to DLVO theory.<sup>27</sup> Replacing these stabilising ligands with reactive molecules often disrupts this balance, leading to uncontrolled aggregation. Additional factors such as organic solvents or reaction additives (e.g.,  $\text{Cu}^+$  in click reactions) can further compromise colloidal stability. Therefore, careful optimisation of reaction conditions is essential before covalent bond formation can be reliably applied to nanoparticle assembly.

In this work, we employ amide bond formation to achieve controlled assembly of AuNPs and systematically optimise reaction conditions to maximise yield. Carboxylic acids react with amines to form amide bonds when activated by 1-ethyl-3-(3-dimethylaminopropyl)carbodiimide (EDC) and *N*-hydroxysuccinimide (NHS) (Scheme 1). In principle, AuNPs can be assembled simply by functionalising particles with carboxyl and amine groups and reacting them in the presence of EDC and NHS. This approach is widely used to conjugate biomolecules such as proteins and antibodies to AuNPs immobilised on solid substrates for sensing.<sup>17–19</sup> However, its application to nanoparticle–nanoparticle assembly with high yield has rarely been realised, mainly due to the stability issues discussed above. Previous studies have demonstrated the feasibility of covalent nanoparticle assembly through amide bond formation, but these efforts typically resulted in low yields or focused on observation of amide bond formation rather than achieving

controlled, high-throughput assembly.<sup>28–30</sup> Here, we establish a reliable procedure for assembling AuNPs through robust amide linkages. By identifying the key parameters governing this delicate assembly process, we achieve near-quantitative yields of diverse AuNP nanoassemblies.

## Results and discussion

### Strategy for assembly through amide bond formation

Fig. 2 illustrates the overall strategy for assembling AuNPs through amide bond formation. The detailed procedure is described in the Experimental section, and the rationale for ligand selection and optimisation is discussed in the following subsections. In this approach, one component of the assembly is immobilised on a glass substrate, which offers two advantages: (i) nanoparticle surfaces can be modified without aggregation or destabilisation—a common issue during ligand exchange in solution—and (ii) unreacted reagents can be efficiently removed by washing.<sup>31</sup>

To immobilise AuNPs, glass substrates were first coated with 3-aminopropyltrimethoxysilane (APTMS), producing positively charged surfaces (Fig. 2a(i)). Negatively charged AuNPs—such as citrate-capped nanospheres (cit-AuNSs) or cetyltrimethylammonium (CTA)-capped nanocubes (CTA-AuNCs)—were then electrostatically adsorbed (Fig. 2a(ii)).<sup>32</sup> Notably, CTA-AuNCs reverse their surface charge from positive to negative when dispersed in 80–90% acetonitrile, as reported previously.<sup>33,34</sup> The immobilised nanoparticles are hereafter referred to as the core particles (in contrast to the satellite particles introduced later), reflecting their position within the final assembly structures. The surfaces of the core AuNPs were subsequently



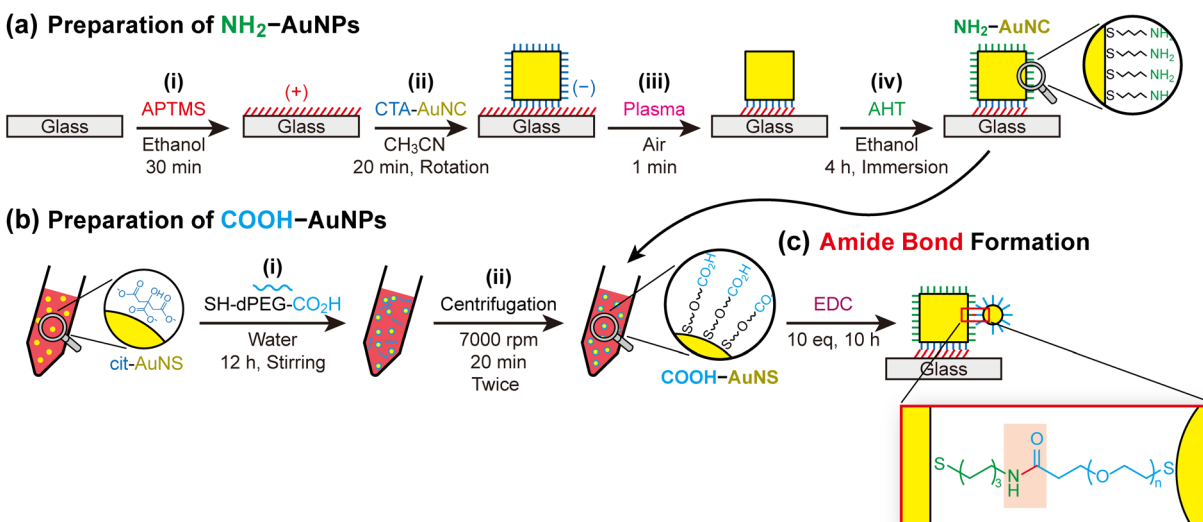


**Fig. 2** Strategy for assembling AuNPs *via* amide bond formation. (a) Preparation of amine-functionalised AuNPs ( $\text{NH}_2\text{-AuNPs}$ ) on glass substrates: (i) coating glass substrates with APTMS to generate positively charged surfaces; (ii) electrostatic adsorption of negatively charged AuNPs (e.g., acetonitrile-treated CTA-AuNCs); (iii) plasma cleaning of both AuNP and substrate surfaces; (iv) functionalisation with AHT to produce  $\text{NH}_2\text{-AuNPs}$ . (b) Preparation of carboxyl-functionalised AuNPs ( $\text{COOH-AuNPs}$ ): (i) ligand exchange of cit-AuNPs with  $\text{SH-dPEG-COOH}$  to introduce terminal carboxyl groups; (ii) purification by repeated centrifugation to remove unbound ligands, with PEG spacers ensuring colloidal stability. (c) Final assembly of  $\text{COOH-AuNPs}$  with  $\text{NH}_2\text{-AuNPs}$  on glass substrates in the presence of EDC, yielding covalent interparticle amide bonds (red).

cleaned with plasma and functionalised with 6-amino-1-hexanethiol (AHT), producing amine-terminated core AuNPs ( $\text{NH}_2\text{-AuNPs}$ ) (Fig. 2a(iii and iv)).

Direct addition of amino-thiols ( $\text{NH}_2\text{-R-SH}$ ) to dispersed cit-AuNSs causes severe aggregation because protonated amines cross-link the negatively charged citrate-stabilised nanoparticles.<sup>35</sup> Immobilisation on glass is therefore essential for converting citrate-capped surfaces into amine-terminated ones while maintaining colloidal stability.

Carboxyl-functionalised AuNPs ( $\text{COOH-AuNPs}$ ), which serve as the coupling partners for  $\text{NH}_2\text{-AuNPs}$ , were prepared by mixing cit-AuNSs with thiolated PEG molecules of discrete molecular weight ( $\text{SH-dPEG-COOH}$ ) (Fig. 2b(i)). The thiol groups chemisorb onto the Au surfaces, replacing the citrate ligands, and the exposed termini provide carboxyl functionality. Removing unbound  $\text{SH-dPEG-COOH}$  is critical for high-yield assembly because free ligands can react prematurely with surface amines on the core particles (Fig. 2b(ii)). Importantly, the hydrophilic PEG backbone imparts sufficient colloidal stability to withstand repeated centrifugation, which is required for purification.<sup>36,37</sup>

Assembly was achieved by immersing  $\text{NH}_2\text{-AuNP/glass}$  substrates in  $\text{COOH-AuNP}$  solutions, followed by immediate addition of EDC and NHS (Fig. 2c). The EDC concentration was controlled to  $\sim 10$  equivalents (eq) relative to the estimated number of carboxyl groups on  $\text{COOH-AuNPs}$ . The reaction was allowed to proceed for 10 h.

The resulting core@satellite assemblies were characterised by UV-vis spectroscopy, scanning electron microscopy (SEM), and transmission electron microscopy (TEM). The assembly yield—determined from SEM analysis—was defined as the

fraction of core particles on the substrate that successfully formed assemblies.

### Selection of $\text{NH}_2$ ligands

The assembly strategy outlined in Fig. 2 was refined by systematically evaluating key experimental parameters at each step (Fig. 3). For amine functionalisation, only a limited number of amino-thiol compounds were suitable. Among linear alkylamines ( $\text{NH}_2(\text{CH}_2)_n\text{SH}$ ), cysteamine ( $n = 2$ ) fails to form stable self-assembled monolayers (SAMs) on AuNP surfaces due to its short alkyl chain.<sup>38,39</sup> At the opposite extreme, 11-amino-1-undecanethiol ( $n = 11$ ) forms stable SAMs, but is prohibitively expensive. Accordingly, AHT ( $n = 6$ ) was selected as a practical compromise between stability and cost.

We also examined aromatic amino-thiols, represented by 4-aminobenzenethiol (ABT), which is frequently used in surface-enhanced Raman spectroscopy (SERS).<sup>40</sup> Comparative experiments revealed that AHT is a far more effective amine ligand than ABT in the EDC coupling reaction: AHT-functionalised AuNPs exhibited assembly yields exceeding 90%, whereas ABT-functionalised AuNPs yielded less than 15% (Fig. 3a). This contrast likely arises from differences in amine basicity. The  $\text{pK}_a$  of AHT is approximately 10.6, whereas that of ABT is 4.9.<sup>41</sup> Consequently, ABT is substantially less nucleophilic at the operating pH  $\approx 5.0$ , reducing its reactivity towards the activated carboxyl groups and resulting in a lower assembly yield.

### Selection of $\text{COOH}$ ligands

A critical factor in preparing  $\text{COOH-AuNPs}$  is the complete removal of residual carboxyl-thiol ligands after surface



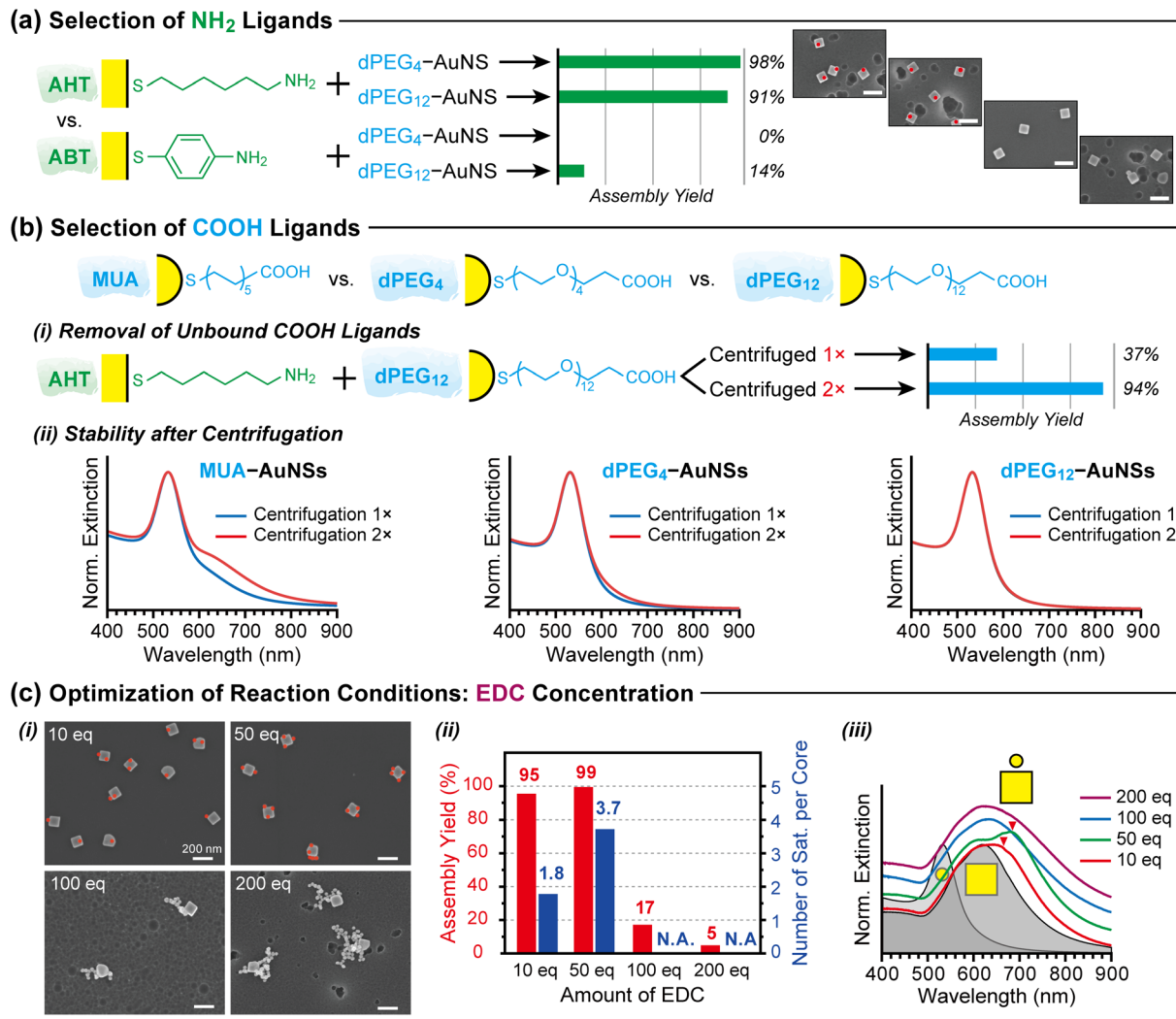


**Fig. 3** Optimisation of AuNP assembly via amide bond formation. (a) Selection of amine ligands. Assembly yields (green bar graphs) are compared among the assemblies where AHT- or ABT-functionalised  $\text{AuNC}_{93}$  cores are coupled with COOH-functionalised  $\text{AuNS}_{35}$  satellites in the presence of EDC. AHT affords markedly higher yields than ABT. Representative SEM images are shown, with  $\text{AuNS}_{35}$  satellites false-coloured red for clarity. (b) Selection of carboxyl ligands. Three ligands—MUA, dPEG<sub>4</sub>, and dPEG<sub>12</sub>—were tested. (i) Assembly yields increase substantially when residual dPEG<sub>12</sub> is removed from the dPEG<sub>12</sub> + cit-AuNS<sub>35</sub> solution by centrifugation prior to coupling with  $\text{NH}_2\text{-AuNC}_{93}$ . (ii) Stability comparison showing that PEG-based ligands (dPEG<sub>4</sub>, dPEG<sub>12</sub>) maintain colloidal stability after two centrifugation cycles, whereas MUA-functionalised  $\text{AuNS}_{35}$  destabilise. (c) Optimisation of EDC concentration. (i) SEM images of  $\text{AuNC}_{101}@\text{AuNS}_{35}$  assemblies formed with 10–200 eq. of EDC relative to surface carboxyl groups. (ii) Quantification of assembly yields and average satellite number per core as a function of EDC concentration. (iii) Normalised UV-vis spectra of assemblies prepared at different EDC concentrations. Red triangles denote plasmon coupling bands. Grey-filled curves show the LSPR spectra of the individual building blocks (AuNC and AuNS) for comparison. Spectra are vertically offset for clarity. Scale bar: 200 nm.

attachment. Free ligands remaining in solution not only react with EDC to form urea byproducts but also compete with surface-bound ligands by rapidly reacting with  $\text{NH}_2\text{-AuNPs}$ , thereby suppressing the desired interparticle coupling. Repeated centrifugation markedly improved assembly yields by removing these unbound ligands (Fig. 3b(i)).

However, repeated centrifugation can compromise the stability of COOH-AuNPs. Most commercially available mercaptoalkanoic acids ( $\text{SH}(\text{CH}_2)_n\text{COOH}$ ;  $n = 2, 5, 7, 10, 11, 15$ ), exemplified by 11-mercaptopoundecanoic acid (MUA,  $n = 11$ ), destabilise rapidly after multiple centrifugation cycles (Fig. 3b(ii)). In contrast, AuNPs functionalised with carboxyl

ligands bearing hydrophilic PEG spacers remain stable under the same conditions (Fig. 3b(ii)). Zeta potential measurements confirm that PEG-based ligands provide equal or superior colloidal stability compared with cit-AuNPs and MUA-AuNPs (Table S1). For this reason, we employed PEGylated carboxyl-thiols with discrete molecular weights (“dPEG<sub>n</sub>” =  $\text{SH}(\text{CH}_2\text{-CH}_2\text{O})_n\text{CH}_2\text{CH}_2\text{COOH}$ ,  $n = 4, 12$ ) to prepare COOH-AuNPs.

### Optimisation of reaction conditions

After preparing COOH-AuNPs and immobilising  $\text{NH}_2\text{-AuNPs}$  on glass substrates, the substrates were immersed in COOH-AuNP solutions containing EDC and NHS for 10 h. To determine the

optimal EDC concentration, we estimated the number of carboxyl groups on COOH-AuNPs by assuming an occupation area of  $0.25 \text{ nm}^2$  per SH-dPEG-COOH ligand<sup>39</sup> and calculating the total surface area of AuNPs ( $2.8 \times 10^{-10} \text{ M} \times 30 \text{ mL} \times N_A \times 4\pi(17.6 \text{ nm})^2$ ). Based on this estimate, the EDC concentration was varied from 10 to 200 eq. relative to carboxyl groups.

Representative SEM images (Fig. 3c(i)) show core@satellite assemblies formed by combining AHT-functionalised AuNC<sub>101</sub> cores with dPEG<sub>12</sub>-AuNS<sub>35</sub> satellites at different EDC concentrations. Both 10 eq. and 50 eq. of EDC produced well-defined core@satellite structures; however, the number of satellites differed. At 10 eq, assemblies typically contained one or two AuNS satellites per AuNC core, whereas at 50 eq, three or more satellites were commonly observed (Fig. 3c(ii)). Additional SEM images are provided in the SI (Fig. S1).

UV-vis spectra further support these findings. Both assemblies exhibit redshifted plasmon coupling bands relative to the localised surface plasmon resonance (LSPR) peaks of the individual building blocks (grey-filled curves), with more pronounced shifts at 50 eq. (Fig. 3c(iii)). The extent of the redshift is known to scale with the number of satellite nanoparticles per core.<sup>42,43</sup>

These results indicate that a moderate excess of EDC ( $\approx 10$  eq.) is necessary to effectively activate carboxyl groups and

promote amide-bond formation with surface amines. Increasing the EDC concentration to 50 eq. enhances the number of activated carboxylates, thereby increasing the frequency of productive amide coupling events and the number of satellites attached per core.

By contrast, higher EDC concentrations (100–200 eq.) lead to uncontrolled aggregation, as evidenced by irregular clusters in SEM images (Fig. 3c(i)). The corresponding UV-vis spectra show broad, strongly redshifted bands characteristic of extensive plasmon coupling across multiple nanoparticles (Fig. 3c(iii)). We attribute this aggregation primarily to the increased ionic strength caused by excess EDC·HCl, which screens electrostatic repulsion between nanoparticles and destabilises the colloid in accordance with DLVO theory.

### Optical and structural properties of the nanoassemblies

After optimising the reaction conditions, we assembled different building blocks into core@satellite nanostructures. Fig. 4a–e present representative assemblies along with their optical and structural properties.

As core particles (green boxes), we used CTA-capped AuNC<sub>93</sub> (edge length:  $93.4 \pm 2.4 \text{ nm}$ ) and highly spherical AuNS<sub>69</sub>

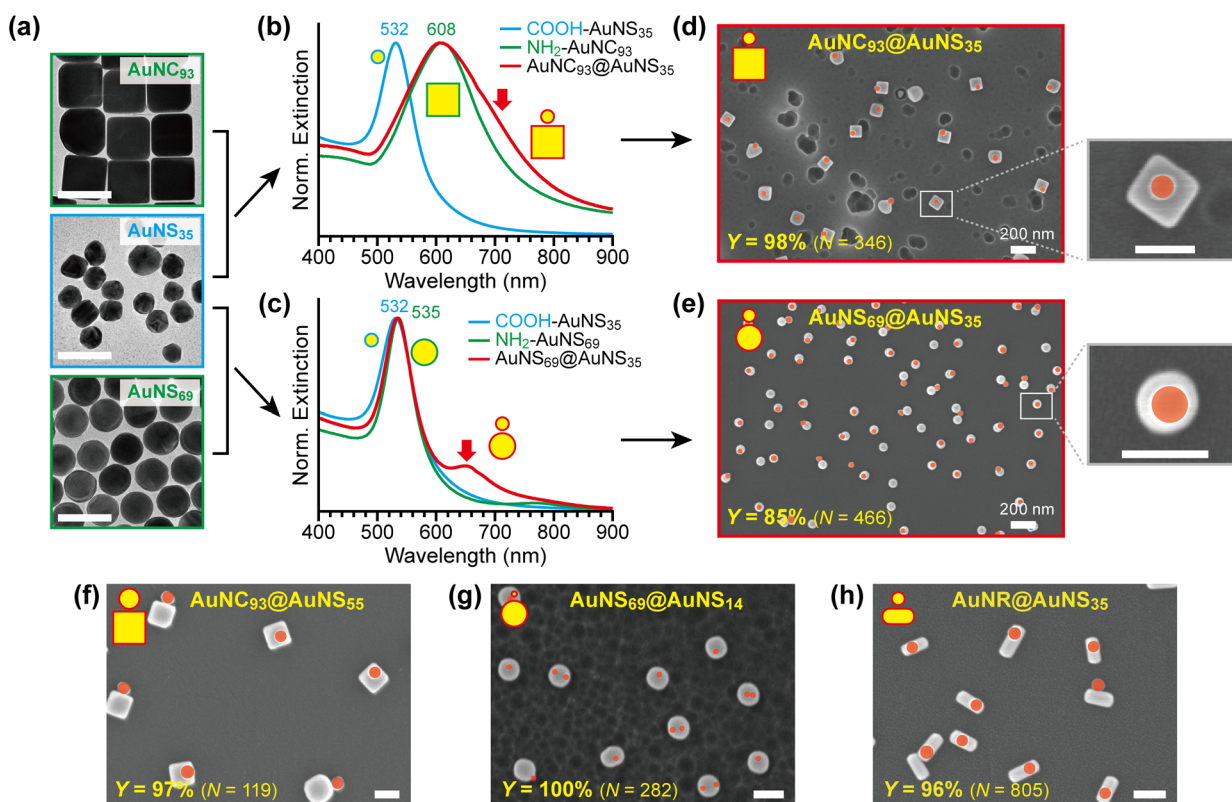


Fig. 4 Assembly of AuNPs through amide bond formation, showing (a–e) the optical and structural properties of representative core@satellite assemblies and (f–h) the extension of the method to diverse AuNP combinations. (a) TEM images of the individual building blocks: AuNC<sub>93</sub> (top), AuNS<sub>35</sub> (middle), and AuNS<sub>69</sub> (bottom). (b and c) Normalised UV-vis extinction spectra of the nanoassemblies (AuNC<sub>93</sub>@AuNS<sub>35</sub> and AuNS<sub>69</sub>@AuNS<sub>35</sub>, red) compared with their corresponding building blocks (COOH-AuNS<sub>35</sub>, cyan; NH<sub>2</sub>-AuNC<sub>93</sub> and NH<sub>2</sub>-AuNS<sub>69</sub>, green). Red arrows mark the plasmon coupling bands. (d and e) SEM images of AuNC<sub>93</sub>@AuNS<sub>35</sub> and AuNS<sub>69</sub>@AuNS<sub>35</sub> assemblies, highlighting their structural characteristics: high yield ( $Y$ ), 1 : 1 stoichiometry, and predominantly on-top satellite adsorption. Satellites are false-coloured red for clarity. Insets show magnified views of individual assemblies. (f–h) SEM images of assemblies with varied shapes and sizes, demonstrating the generality of the amide-bond assembly strategy. Unlabeled scale bars represent 100 nm.



(diameter:  $69.4 \pm 1.9$  nm), which were immobilised on glass substrates and functionalised with AHT. As satellite particles (cyan box), we employed citrate-capped, irregularly shaped  $\text{AuNS}_{35}$  (diameter:  $35.2 \pm 3.8$  nm), subsequently functionalised with dPEG<sub>4</sub>. Fig. 4a–c show TEM images and UV-vis extinction spectra of these building blocks.

The LSPR peaks of  $\text{AuNC}_{93}$ ,  $\text{AuNS}_{69}$ , and  $\text{AuNS}_{35}$  appear at 608, 535, and 532 nm, respectively. As these building blocks are assembled through EDC-mediated amide bond formation, plasmonic interactions between cores and satellites give rise to new bonding dipole plasmon modes at longer wavelengths than the LSPR peaks of the individual components, as indicated by the red arrows in Fig. 4b and c.<sup>44</sup> The plasmon coupling band is less pronounced in  $\text{AuNC}_{93}@\text{AuNS}_{35}$  due to the inherently broad LSPR of the AuNCs, but is clearly distinguishable in  $\text{AuNS}_{69}@\text{AuNS}_{35}$ .

The strength of plasmon coupling is highly sensitive to interparticle distance.<sup>45,46</sup> Longer linker lengths weaken the interaction, resulting in smaller redshifts of the coupling bands. Replacing dPEG<sub>4</sub> (length  $\approx 1.8$  nm)<sup>47</sup> with dPEG<sub>12</sub> (length  $\approx 4.7$  nm)<sup>48</sup> on the satellites markedly reduces plasmon coupling, as reflected in weaker and less redshifted bands in the extinction spectra (Fig. S2).

Fig. 4d and e display representative SEM images of the resulting nanoassemblies, with satellites ( $\text{AuNS}_{35}$ ) coloured with red circles for clarity.  $\text{AuNC}_{93}@\text{AuNS}_{35}$  assemblies exhibit a near-quantitative yield of 98% ( $N = 346$ ), whereas  $\text{AuNS}_{69}@\text{AuNS}_{35}$  achieve a slightly lower yield of 85% ( $N = 466$ ), likely because the smaller  $\text{AuNS}_{69}$  cores provide less surface area for satellite attachment. Consistent with the optimised conditions (10 eq. of EDC; see Fig. 3c), most assemblies contain only one or two  $\text{AuNS}_{35}$  satellites per core, with satellites preferentially binding to the top surfaces of the cores rather than the sides.

#### Extension of the method to various combinations

We further extended this assembly strategy to a variety of building blocks with different sizes and shapes. For  $\text{AuNC}_{93}@\text{AuNS}_{55}$  assemblies (Fig. 4f), where slightly larger satellites (55 nm) replace  $\text{AuNS}_{35}$ , the assemblies retain the same structural characteristics: 1:1 stoichiometry, high yield (97%), and predominantly on-top adsorption of satellites.

When smaller satellites are used, the assembly yield remains excellent. For example,  $\text{AuNS}_{69}@\text{AuNS}_{14}$  assemblies achieve a 100% yield (Fig. 4g). In these structures, multiple  $\text{AuNS}_{14}$  satellites often adsorb on a single  $\text{AuNS}_{69}$  core, likely because of the increased relative surface area available for adsorption.

The method also proves effective for anisotropic particles. Using gold nanorods (AuNRs) as cores, we obtained assemblies with similarly high yields and well-controlled stoichiometry (Fig. 4h). Additional SEM images are provided in the SI (Fig. S3).

#### Confirmation of amide bonds

The formation of amide bonds was verified by SERS measurements on the core@satellite nanoassemblies. Fig. 5 shows normalised Raman spectra averaged over 22 measurements from three independently prepared  $\text{AuNC}_{101}@\text{AuNS}_{35}$  samples.

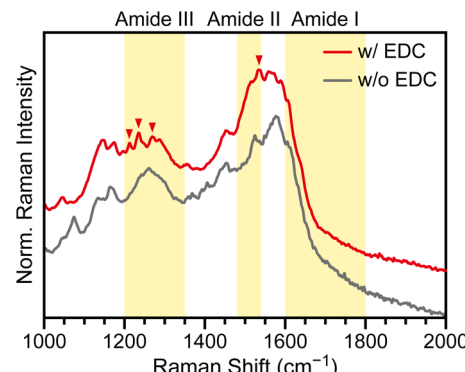


Fig. 5 Confirmation of amide bond formation in AuNP assemblies. The red trace represents the averaged, normalised Raman spectrum from three  $\text{AuNC}_{101}@\text{AuNS}_{35}$  samples assembled with EDC. For comparison, the grey trace shows spectra from control assemblies without EDC. Distinct peaks at 1212, 1235, 1269, and  $1533\text{ cm}^{-1}$  (red triangles) appear only in the EDC-mediated assemblies and fall within the yellow-shaded regions corresponding to amide vibrational modes, confirming covalent linkage between nanoparticles.

The spectra exhibit relatively weak overall intensity with a broad background, but distinct spectral features emerge when compared with control samples.

Control assemblies prepared without EDC also form, but only with low and inconsistent yields, characteristic of nonspecific binding (Fig. S4). In this case, electrostatic attraction between protonated amines and deprotonated carboxylates likely drives the weak association of particles. However, these nonspecific assemblies lack the vibrational signatures of amide bonds (grey trace).

By contrast, EDC-mediated assemblies exhibit distinct new peaks at 1212, 1235, 1269, and  $1533\text{ cm}^{-1}$  (red triangles in Fig. 5). These bands correspond to characteristic vibrational modes of amide bonds (yellow-shaded regions),<sup>28,29,49,50</sup> providing direct spectroscopic evidence for covalent linkages between nanoparticles.

## Experimental section

### Synthesis of building blocks

AuNPs were synthesised following reported protocols: cit-AuNPs (Puntes group),<sup>51</sup> CTA-AuNSs (Xia group),<sup>52</sup> CTA-AuNCs (Nam group),<sup>53</sup> and CTA-AuNRs (Murray group).<sup>54</sup> Detailed procedures are provided in our previous publications. All reagents were purchased from Sigma-Aldrich and used without further purification. The structural and optical properties of the synthesised AuNPs are shown in the SI (Fig. S5).

### Preparation of $\text{NH}_2\text{-AuNPs}$

The amine functionalisation procedure is illustrated in Fig. 2a. To prevent aggregation during ligand exchange, AuNPs were first immobilised on glass substrates.

(i) Amine coating of glass substrates: glass substrates ( $9 \times 12.5$  mm, Marienfeld, Germany) were thoroughly cleaned and immersed in an APTMS/ethanol solution (57 mM, 4 mL) for 30 min.



(ii) Adsorption of core AuNPs: the amine-coated substrates were immersed in a conical tube containing a solution of negatively charged AuNPs (optical density, OD = 0.35, 5 mL). The tube was rotated for 20 min to promote adsorption. Negatively charged AuNPs included cit-AuNPs in water and CTA-AuNPs in 80–90% acetonitrile. The acetonitrile treatment removes the outer CTA bilayer, reversing the  $\zeta$ -potential of the AuNPs from positive to negative.

(iii) Plasma cleaning: the AuNP/glass substrates were plasma-treated (0.8 torr air, 18 W, PDC-32G-2, Harrick Plasma, U.S.A.) for 1 min to remove surface ligands from the AuNPs as well as the amine coating on the glass substrates.

(iv) Amine functionalisation: the cleaned AuNP/glass substrates were immersed in an AHT/ethanol solution (1 mM, 5 mL) for 4 h. As discussed above, ABT was not an effective amine ligand for EDC coupling due to its low  $pK_a$  and reduced basicity.

### Preparation of COOH-AuNPs

To prepare COOH-AuNPs, a cit-AuNP solution (OD = 0.95, 30 mL) was mixed with SH-dPEG-COOH solution (1 mM, 0.84 mL) and stirred for 12 h. The mixture was then centrifuged at 7000 rpm for 20 min to remove unbound SH-dPEG-COOH. After discarding the supernatant, fresh water was added, and the centrifugation step was repeated.

### EDC coupling reaction

After preparing NH<sub>2</sub>-AuNPs on glass substrates and COOH-AuNPs in solution, the two were reacted to form amide bonds. The NH<sub>2</sub>-AuNP/glass substrate was immersed in the COOH-AuNP solution (4-fold diluted, final volume = 5 mL), followed by immediate addition of EDC and NHS. The EDC concentration corresponded to 10 eq. of the estimated number of carboxyl groups on the COOH-AuNPs (10 mM, 7  $\mu$ L). The reaction was allowed to proceed for 10 h at room temperature.

### Measurements

AuNP assemblies were imaged using field-emission SEM (Sigma, Carl Zeiss, Germany). The structure of the AuNP building blocks was characterised by TEM (JEM-F200, JEOL, Japan). Optical properties, including the plasmon resonance of the individual AuNPs and plasmon coupling in assemblies, were measured using UV-vis spectroscopy (Lambda 365+, PerkinElmer, U.S.A.).  $\zeta$ -Potential measurements (Zetasizer, Malvern, U.K.) were performed before and after ligand exchange with carboxyl-thiols to evaluate colloidal stability. Raman spectra were collected from AuNC@AuNS nanoassemblies to confirm amide bond formation using a Raman microscope (RamanRx1, Kaiser Optical Systems, U.S.A.) with 785 nm excitation.

### Conclusions

Although EDC-driven amide coupling is one of the most widely used reactions in bioconjugation and nanoparticle assembly, the authenticity of the resulting covalent bond formation is

rarely questioned. This stems in part from the lack of detailed reports on failure modes, which are crucial for experimentalists attempting reproducible coupling reactions. Here we report a robust general strategy for assembling AuNPs through covalent amide linkages and identify the key parameters governing yield and stability. Surface modification of AuNPs with AHT and SH-dPEG-COOH provides the requisite amine and carboxyl functionalities. Amine functionalisation must be performed on AuNPs immobilised on glass substrates to prevent aggregation, and alkylamines outperform arylamines owing to their higher nucleophilicity and reactivity towards amide formation.

For carboxyl functionalisation, ligand exchange with carboxyl-thiols is effective in dispersion, but removal of unbound ligands by repeated centrifugation is critical for achieving high-yield assembly with NH<sub>2</sub>-AuNPs. Destabilisation of the COOH-AuNPs caused by multiple centrifugation cycles can be mitigated by using SH-dPEG-COOH, which provides additional colloidal stability through its hydrophilic dPEG spacers.

Amide bond formation is promoted by EDC, with 10 eq. relative to surface carboxyl groups, producing nanoassemblies of near-quantitative yield (~100%), 1:1 core-to-satellite stoichiometry, and on-top satellite-on-core configuration. SERS spectra of the resulting assemblies display characteristic amide vibrational peaks, providing direct spectroscopic evidence of covalent linkage. This assembly strategy is broadly applicable, enabling the high-yield preparation of diverse core@satellite structures derived from AuNSs, AuNCs, and AuNRs of various sizes and morphologies. Together, these results deliver not only a high-yield covalent assembly method but also a detailed set of practical guidelines and critical precautions for researchers attempting similar experiments. This strategy thus offers a versatile and reproducible platform for constructing plasmonic nanoassemblies through controlled chemical reactions.

### Author contributions

The manuscript was written through contributions of all authors. All authors have given approval to the final version of the manuscript. The authors contributed to this work as follows: S. H. (data curation, formal analysis, investigation, methodology), Y. L. (data curation, investigation, resources), S. K. (conceptualisation, supervision, writing), S. Y. (conceptualisation, funding acquisition, supervision, writing).

### Conflicts of interest

There are no conflicts to declare.

### Data availability

Data for this article are available at our group OneDrive ([https://nanoplasmatics-my.sharepoint.com/:f/g/personal/sangwoon\\_nanoplasmatics\\_onmicrosoft\\_com/IgDsvsiJIDutT4S9aaHjp6NpAQpXcKjFXz8wrsgKXZor9ow?e=LJtabi](https://nanoplasmatics-my.sharepoint.com/:f/g/personal/sangwoon_nanoplasmatics_onmicrosoft_com/IgDsvsiJIDutT4S9aaHjp6NpAQpXcKjFXz8wrsgKXZor9ow?e=LJtabi)).

Supplementary information (SI):  $\zeta$ -potential of carboxyl-functionalised AuNSs with different ligands; additional SEM images of AuNC@AuNS assemblies at different EDC concentrations; shifts of plasmon coupling bands with decreasing interparticle distance; additional SEM images of diverse AuNP assemblies formed *via* amide bond coupling; yields of nano-assemblies prepared with and without EDC; and structural and optical characteristics of the building blocks. See DOI: <https://doi.org/10.1039/d5sc08787b>.

## Acknowledgements

This work was supported by the National Research Foundation of Korea (RS-2024-00350882 and RS-2020-NR049537). Yeonsoo Lim gratefully acknowledges the support from the Chung-Ang University Graduate Research Scholarship (2024).

## Notes and references

- 1 S. A. Maier, *Plasmonics: Fundamentals and Applications*, Springer, New York, NY, 2007.
- 2 M.-C. Daniel and D. Astruc, Gold Nanoparticles: Assembly, Supramolecular Chemistry, Quantum-Size-Related Properties, and Applications toward Biology, Catalysis, and Nanotechnology, *Chem. Rev.*, 2004, **104**, 293–346.
- 3 J. Zhao, A. O. Pinchuk, J. M. McMahon, S. Li, L. K. Ausman, A. L. Atkinson and G. C. Schatz, Methods for Describing the Electromagnetic Properties of Silver and Gold Nanoparticles, *Acc. Chem. Res.*, 2008, **41**, 1710–1720.
- 4 G. V. Hartland, Optical Studies of Dynamics in Noble Metal Nanostructures, *Chem. Rev.*, 2011, **111**, 3858–3887.
- 5 P. K. Jain, X. Huang, I. H. El-Sayed and M. A. El-Sayed, Noble Metals on the Nanoscale: Optical and Photothermal Properties and Some Applications in Imaging, Sensing, Biology, and Medicine, *Acc. Chem. Res.*, 2008, **41**, 1578–1586.
- 6 K. Kant, R. Beeram, Y. Cao, P. S. S. dos Santos, L. González-Cabaleiro, D. García-Lojo, H. Guo, Y. Joung, S. Kothadiya, M. Lafuente, *et al.*, Plasmonic Nanoparticle Sensors: Current Progress, Challenges, and Future Prospects, *Nanoscale Horiz.*, 2024, **9**, 2085–2166.
- 7 J. Zeng, Y. Zhang, T. Zeng, R. Aleisa, Z. Qiu, Y. Chen, J. Huang, D. Wang, Z. Yan and Y. Yin, Anisotropic Plasmonic Nanostructures for Colorimetric Sensing, *Nano Today*, 2020, **32**, 100855.
- 8 S. Schlücker, Surface-Enhanced Raman Spectroscopy: Concepts and Chemical Applications, *Angew. Chem., Int. Ed.*, 2014, **53**, 4756–4795.
- 9 Y. Zhang, W. Guo, Y. Zhang and W. D. Wei, Plasmonic Photoelectrochemistry: In View of Hot Carriers, *Adv. Mater.*, 2021, **33**, 2006654.
- 10 Y. H. Jang, Y. J. Jang, S. Kim, L. N. Quan, K. Chung and D. H. Kim, Plasmonic Solar Cells: From Rational Design to Mechanism Overview, *Chem. Rev.*, 2016, **116**, 14982–15034.
- 11 Y. Wu, M. R. K. Ali, B. Dong, T. Han, K. Chen, J. Chen, Y. Tang, N. Fang, F. J. Wang and M. A. El-Sayed, Gold Nanorod Photothermal Therapy Alters Cell Junctions and Actin Network in Inhibiting Cancer Cell Collective Migration, *ACS Nano*, 2018, **12**, 9279.
- 12 M. Rycenga, C. M. Cobley, J. Zeng, W. Li, C. H. Moran, Q. Zhang, D. Qin and Y. Xia, Controlling the Synthesis and Assembly of Silver Nanostructures for Plasmonic Applications, *Chem. Rev.*, 2011, **111**, 3669–3712.
- 13 N. J. Halas, S. Lal, W.-S. Chang, S. Link and P. Nordlander, Plasmons in Strongly Coupled Metallic Nanostructures, *Chem. Rev.*, 2011, **111**, 3913–3961.
- 14 L. V. Besteiro and A. O. Govorov, Amplified Generation of Hot Electrons and Quantum Surface Effects in Nanoparticle Dimers with Plasmonic Hot Spots, *J. Phys. Chem. C*, 2016, **120**, 19329–19339.
- 15 C. E. Talley, J. B. Jackson, C. Oubre, N. K. Grady, C. W. Hollars, S. M. Lane, T. R. Huser, P. Nordlander and N. J. Halas, Surface-Enhanced Raman Scattering from Individual Au Nanoparticles and Nanoparticle Dimer Substrates, *Nano Lett.*, 2005, **5**, 1569–1574.
- 16 A. Rao, S. Roy, V. Jain and P. P. Pillai, Nanoparticle Self-Assembly: From Design Principles to Complex Matter to Functional Materials, *ACS Appl. Mater. Interfaces*, 2023, **15**, 25248–25274.
- 17 K. E. Sapsford, W. R. Algar, L. Berti, K. B. Gemmill, B. J. Casey, E. Oh, M. H. Stewart and I. L. Medintz, Functionalizing Nanoparticles with Biological Molecules: Developing Chemistries That Facilitate Nanotechnology, *Chem. Rev.*, 2013, **113**, 1904–2074.
- 18 M. A. Nash, J. N. Waitumbi, A. S. Hoffman, P. Yager and P. S. Stayton, Multiplexed Enrichment and Detection of Malarial Biomarkers Using a Stimuli-Responsive Iron Oxide and Gold Nanoparticle Reagent System, *ACS Nano*, 2012, **6**, 6776–6785.
- 19 P. P. Joshi, S. J. Yoon, W. G. Hardin, S. Emelianov and K. V. Sokolov, Conjugation of Antibodies to Gold Nanorods through Fc Portion: Synthesis and Molecular Specific Imaging, *Bioconjugate Chem.*, 2013, **24**, 878–888.
- 20 A. C. Cardiel, M. C. Benson, L. M. Bishop, K. M. Louis, J. C. Yeager, Y. Z. Tan and R. J. Hamers, Chemically Directed Assembly of Photoactive Metal Oxide Nanoparticle Heterojunctions Via the Copper-Catalyzed Azide-Alkyne Cycloaddition “Click” Reaction, *ACS Nano*, 2012, **6**, 310–318.
- 21 N. Gandra and S. Singamaneni, “Clicked” Plasmonic Core-Satellites: Covalently Assembled Gold Nanoparticles, *Chem. Commun.*, 2012, **48**, 11540–11542.
- 22 M. Dolci, D. Toulemon, Z. Chaffar, J. L. Bubendorff, F. Tielens, M. Calatayud, S. Zafeiratos, S. Begin-Colin and B. P. Pichon, Nanoparticle Assembling through Click Chemistry Directed by Mixed Sams for Magnetic Applications, *ACS Appl. Nano Mater.*, 2019, **2**, 554–565.
- 23 A. Dabbous, P. Bauer, C. Marcucci, S. Périé, S. Gahlot, C. Lombard, S. Caillat, J. L. Ravanat, J. M. Mouesca, S. Kodjikian, *et al.*, Hybrid CdSe/ZnS Quantum Dot-Gold Nanoparticle Composites Assembled by Click Chemistry: Toward Affordable and Efficient Redox Photocatalysts Working with Visible Light, *ACS Appl. Mater. Interfaces*, 2023, **15**, 56167–56180.



24 R. K. Gupta, D. Y. Kusuma, P. S. Lee and M. P. Srinivasan, Covalent Assembly of Gold Nanoparticles for Nonvolatile Memory Applications, *ACS Appl. Mater. Interfaces*, 2011, **3**, 4619–4625.

25 T. Gumabat, J. P. L. Oracion, J. Fedelis, E. Keleste, R. Capangpangan, N. L. Sayson, G. Dumancas, A. Alguno and F. Latayada, NHS-Ester Conjugated Gold Nanoparticles for Spermine Detection: A Potential Tool in Meat Spoilage Monitoring, *Sens. Diagn.*, 2025, **4**, 182–194.

26 S. Borsley and E. R. Kay, Dynamic Covalent Assembly and Disassembly of Nanoparticle Aggregates, *Chem. Commun.*, 2016, **52**, 9117–9120.

27 G. Cao, *Nanostructures & Nanomaterials: Synthesis, Properties & Applications*, Imperial College Press, London, 2004.

28 D. S. Indrasekara, A. Swarnapali, R. Thomas and L. Fabris, Plasmonic Properties of Regiospecific Core-Satellite Assemblies of Gold Nanostars and Nanospheres, *Phys. Chem. Chem. Phys.*, 2015, **17**, 21133–21142.

29 N. Kong, J. Guo, S. Chang, J. Pan, J. Wang, J. Zhou, J. Liu, H. Zhou, F. M. Pfeffer, J. Liu, *et al.*, Direct Observation of Amide Bond Formation in a Plasmonic Nanocavity Triggered by Single Nanoparticle Collisions, *J. Am. Chem. Soc.*, 2021, **143**, 9781–9790.

30 T. J. Yim, Y. Wang and X. Zhang, Synthesis of a Gold Nanoparticle Dimer Plasmonic Resonator through Two-Phase-Mediated Functionalization, *Nanotechnology*, 2008, **19**, 435605.

31 H. D. Trinh, S. Kim, S. Yun, L. T. M. Huynh and S. Yoon, Combinatorial Approach to Find Nanoparticle Assemblies with Maximum Surface-Enhanced Raman Scattering, *ACS Appl. Mater. Interfaces*, 2024, **16**, 1805–1814.

32 R. G. Freeman, K. C. Grabar, K. J. Allison, R. M. Bright, J. A. Davis, A. P. Guthrie, M. B. Hommer, M. A. Jackson, P. C. Smith, D. G. Walter, *et al.*, Self-Assembled Metal Colloid Monolayers: An Approach to SERS Substrates, *Science*, 1995, **267**, 1629–1632.

33 P. Pramod, S. T. S. Joseph and K. G. Thomas, Preferential End Functionalization of Au Nanorods through Electrostatic Interactions, *J. Am. Chem. Soc.*, 2007, **129**, 6712–6713.

34 P. Pramod and K. G. Thomas, Plasmon Coupling in Dimers of Au Nanorods, *Adv. Mater.*, 2008, **20**, 4300–4305.

35 J. H. Yoon, J. S. Park and S. Yoon, Time-Dependent and Symmetry-Selective Charge-Transfer Contribution to SERS in Gold Nanoparticle Aggregates, *Langmuir*, 2009, **25**, 12475–12480.

36 E. E. Foos, A. W. Snow, M. E. Twigg and M. G. Ancona, Thiol-Terminated Di-, Tri-, and Tetraethylene Oxide Functionalized Gold Nanoparticles: A Water-Soluble, Charge-Neutral Cluster, *Chem. Mater.*, 2002, **14**, 2401–2408.

37 S. Nam, D. V. Parikh, B. D. Condon, Q. Zhao and M. Yoshioka-Tarver, Importance of Poly(Ethylene Glycol) Conformation for the Synthesis of Silver Nanoparticles in Aqueous Solution, *J. Nanopart. Res.*, 2011, **13**, 3755–3764.

38 M. Wirde and U. Gelius, Self-Assembled Monolayers of Cystamine and Cysteamine on Gold Studied by XPS and Voltammetry, *Langmuir*, 1999, **15**, 6370–6378.

39 J. C. Love, L. A. Estroff, J. K. Kriebel, R. G. Nuzzo and G. M. Whitesides, Self-Assembled Monolayers of Thiolates on Metals as a Form of Nanotechnology, *Chem. Rev.*, 2005, **105**, 1103–1170.

40 Y.-F. Huang, H.-P. Zhu, G.-K. Liu, D.-Y. Wu, B. Ren and Z.-Q. Tian, When the Signal Is Not from the Original Molecule to Be Detected: Chemical Transformation of *Para*-Aminothiophenol on Ag During the SERS Measurement, *J. Am. Chem. Soc.*, 2010, **132**, 9244–9246.

41 *CRC Handbook of Chemistry and Physics*, ed. W. M. Haynes, CRC Press, Boca Raton, FL, 95th edn, 2014.

42 J. H. Yoon and S. Yoon, Effects of the Number of Satellites on Surface Plasmon Coupling of Core-Satellite Nanoassemblies, *Bull. Korean Chem. Soc.*, 2013, **34**, 33–34.

43 B. M. Ross, J. R. Waldeisen, T. Wang and L. P. Lee, Strategies for Nanoplasmonic Core-Satellite Biomolecular Sensors: Theory-Based Design, *Appl. Phys. Lett.*, 2009, **95**, 193112.

44 J. H. Yoon, J. Lim and S. Yoon, Controlled Assembly and Plasmonic Properties of Asymmetric Core-Satellite Nanoassemblies, *ACS Nano*, 2012, **6**, 7199–7208.

45 P. K. Jain, W. Huang and M. A. El-Sayed, On the Universal Scaling Behavior of the Distance Decay of Plasmon Coupling in Metal Nanoparticle Pairs: A Plasmon Ruler Equation, *Nano Lett.*, 2007, **7**, 2080–2088.

46 B. M. Reinhard, M. Siu, H. Agarwal, A. P. Alivisatos and J. Liphardt, Calibration of Dynamic Molecular Rulers Based on Plasmon Coupling between Gold Nanoparticles, *Nano Lett.*, 2005, **5**, 2246–2252.

47 Vector Laboratories, Thiol-dPEG<sub>4</sub>-Acid Product Datasheet, <https://vectorlabs.com/productattachments/datasheets/QBD-10247.pdf> (accessed 2025 Aug 27).

48 Vector Laboratories, Thiol-dPEG<sub>12</sub>-Acid Product Datasheet, <https://vectorlabs.com/productattachments/datasheets/QBD-10850.pdf> (accessed 2025 Aug 27).

49 C. Gullekson, L. Lucas, K. Hewitt and L. Kreplak, Surface-Sensitive Raman Spectroscopy of Collagen I Fibrils, *Biophys. J.*, 2011, **100**, 1837–1845.

50 A. K. Tobias and M. Jones, Metal-Enhanced Fluorescence from Quantum Dot-Coupled Gold Nanoparticles, *J. Phys. Chem. C*, 2019, **123**, 1389–1397.

51 N. G. Bastús, J. Comenge and V. Puntes, Kinetically Controlled Seeded Growth Synthesis of Citrate-Stabilized Gold Nanoparticles of up to 200 nm: Size Focusing Versus Ostwald Ripening, *Langmuir*, 2011, **27**, 11098–11105.

52 Y. Zheng, X. Zhong, Z. Li and Y. Xia, Successive, Seed-Mediated Growth for the Synthesis of Single-Crystal Gold Nanospheres with Uniform Diameters Controlled in the Range of 5–150 nm, *Part. Part. Syst. Charact.*, 2014, **31**, 266–273.

53 J. E. Park, Y. Lee and J. M. Nam, Precisely Shaped, Uniformly Formed Gold Nanocubes with Ultrahigh Reproducibility in Single-Particle Scattering and Surface-Enhanced Raman Scattering, *Nano Lett.*, 2018, **18**, 6475–6482.

54 X. Ye, C. Zheng, J. Chen, Y. Gao and C. B. Murray, Using Binary Surfactant Mixtures to Simultaneously Improve the Dimensional Tunability and Monodispersity in the Seeded Growth of Gold Nanorods, *Nano Lett.*, 2013, **13**, 765–771.

